Materials Science & Engineering A 869 (2023) 144831

Contents lists available at ScienceDirect

Materials Science & Engineering A

journal homepage: www.elsevier.com/locate/msea

Thermomechanical fatigue of additively manufactured 316L stainless steel

T. Babinský [a,*], I. Šulák [a], I. Kuběna [a], J. Man [a], A. Weiser [a], E. Švábenská [a], L. Englert [b], S. Guth [b]

[a] Institute of Physics of Materials, Czech Academy of Sciences, Žižkova 22, 616 00, Brno, Czech Republic
[b] Karlsruhe Institute of Technology, IAM-WK Institute for Applied Materials, Engelbert-Arnold-Straße 4, 76131, Karlsruhe, Germany

ARTICLE INFO

Keywords:
Additive manufacturing
Laser powder bed fusion
Thermomechanical fatigue
Stainless steel
316L

ABSTRACT

An important issue in energy conversion is the performance of materials under complex cyclic loading in a variable temperature field. The present study addresses a new field of research – thermomechanical fatigue of additively manufactured metallic materials, which is crucial for understanding the behaviour of this promising material class under real operating conditions. The material of interest – 316L austenitic stainless steel, commonly used for heat exchangers – was manufactured to bars using laser powder bed fusion. Cylindrical specimens with characteristic hierarchical, non-equilibrium cellular microstructure were machined out of the bars. Two orientations corresponding to the inclination of the building direction to the specimen axis were considered: 0° and 90°. The specimens were subjected to thermomechanical fatigue loading under *in-phase* (maximum tension coincides with maximum temperature) and *out-of-phase* (maximum compression coincides with maximum temperature) conditions. The cellular dislocation microstructure showed good stability despite gradual coarsening under the combined effect of thermal loading up to 750 °C and severe plastic deformation. Systematic electron microscopy observations further revealed that basic damage mechanisms – either creep or stress-assisted oxide cracking, the prevalence of which depends on thermomechanical loading conditions – correspond to the behaviour of conventional metallic materials. Under *in-phase* loading, intergranular creep damage is dominant, hence a key factor affecting the lifetime is the number of grain boundaries in the loading direction. Under *out-of-phase* loading, fatigue damage is dominant, and the lifetime is determined by trans-granular propagation of a principal crack. Comparing the two orientations, the inherent microstructural texture was found to be a crucial factor, also determining the number of grain boundaries and cell walls in the loading direction. Hence, tailoring the microstructure for the service relevant loading conditions via additive manufacturing techniques enables to enhance the component performance in the important field of energy conversion.

1. Introduction

The desire to reach sustainable energy conversion has driven the development of new materials, as well as technologies, for years. Projects with game-changing potential, such as ITER in France, demand complex-shaped components manufactured from materials able to withstand extreme operating conditions with steep temperature gradients. Regarding the component manufacturing, a promising candidate is additive manufacturing (AM) which provides design freedom as well as waste minimization. It has been shown [1–3] that by careful process optimization, a unique, highly non-equilibrium and almost defect-less microstructure can be achieved which is accountable for mechanical properties superior to those of conventionally manufactured materials. However, the main factor hindering a wider use in real applications is the limited knowledge concerning mechanical properties and behaviour under complex cyclic loading such as fatigue in a variable temperature field.

Notably, over 90% of premature cracking in mechanically loaded components occurs due to material fatigue. Despite excessive research in the field of AM, very little attention has been paid to the research of

Abbreviations: AM, Additive manufacturing; TMF, Thermomechanical fatigue; L-PBF, Laser powder bed fusion; LA, Loading axis; BD, Building direction; SEM, Scanning electron microscope; EDS, Energy-dispersive spectrometer; EBSD, Electron backscatter diffraction; TEM, Transmission electron microscope; STEM, Scanning transmission electron microscope; HAGB, High-angle grain boundary; LAGB, Low-angle grain boundary; IP, In-phase; OP, Out-of-phase; IPF, Inverse pole figure; SAED, Selected area diffraction.

* Corresponding author.
E-mail address: babinsky@ipm.cz (T. Babinský).

https://doi.org/10.1016/j.msea.2023.144831
Received 29 December 2022; Received in revised form 9 February 2023; Accepted 22 February 2023
Available online 24 February 2023

fatigue properties of AM materials. Only recently, the phenomena of fatigue and related mechanisms in AM metals have been addressed [4–7]. With a surface finish [8], it appears that AM metals perform better than their conventional counterparts not only under quasi-static loading (see e.g. Refs. [1,3]), but also under cyclic loading at temperatures when the fatigue damage is dominant [7]. In energy and petrochemical industry as well as in jet engines, thermomechanical fatigue (TMF) combining the effects of mechanical and thermal cycling arises due to repeated start-stop operations in critical hot-going components such as boilers, turbines, or combustion chambers. Furthermore, high temperature exposure and harsh environmental conditions induce creep and oxidation damage. The interaction of fatigue, creep and oxidation mechanisms during TMF governs often the lifetime of the hot-going components, which is typically in the low cycle fatigue range. Regarding the TMF performance of an AM material, several factors need to be taken into account due to the complexity of TMF loading and AM processes: (i) microstructural texture, (ii) solute segregation [1], (iii) porosity, especially the extremely harmful lack-of-fusion defects [9], (iv) surface integrity since fatigue cracks usually initiate at the surface [10,11], (v) thermodynamical state since the AM metals accumulate residual stresses which can be annealed out by subsequent heat treatment [12], (vi) occurrence of dwells at high temperatures [13,14], (vii) temperature range and (viii) maximum temperature [15,16] and finally (ix) phase angle between the mechanical and thermal cycling [17,18]. In TMF testing, two limit cases of phase angle are usually considered; 180° standing for *out-of-phase* TMF and 0° standing for *in-phase* TMF. Fig. 1 schematically shows the origin of TMF for both loading modes under real operating conditions. As thermal expansion imposes compressive stresses in a hot part of the component, *out-of-phase* TMF, i.e., the maximum temperature coincides with maximum compression, arises. On the other hand, tensile stresses in a cooled part of the component give rise to *in-phase* TMF, i.e., the maximum temperature coincides with maximum tension. For polycrystalline materials, *in-phase* loading produces typically intergranular damage when the maximum temperature exceeds a critical value, while *out-of-phase* loading leads to mainly transgranular damage [13,15,17,18]. Intergranular cracking under *in-phase* loading is usually related to cavity damage on grain boundaries due to the combination of high temperature and tensile stress. When intergranular damage dominates under *in-phase* loading, the resulting lifetime is usually shorter than the respective *out-of-phase* lifetime [13,15,18]. On the other hand, when intergranular damage is absent under *in-phase* loading, *out-of-phase* loading yields typically lower lifetimes [19,20].

Although deeply researched for conventionally manufactured materials, TMF is not fully understood. In particular, the influence of phase angle on TMF lifetime depends significantly on microstructure and is difficult to predict, compare e.g. the results in Refs. [13,17,18]. The unique microstructure of AM metals opens a new field of research, which can contribute to better understanding of TMF in general. Isothermal fatigue tests on AM steels have shown that the specimen orientation relative to the building direction significantly affects the resulting lifetimes [8]. Under TMF loading, similar trends may be expected, particularly with respect to the different damage mechanisms under *in-phase* and *out-of-phase* loading.

Up today, only few works addressed TMF of AM metals. In Ref. [21], the influence of AM parameters, graded microstructures and optional heat treatments on the *in-phase* TMF lifetime were studied for Ni-base superalloy IN718. Lindström et al. [22] investigated and simulated the deformation behaviour of a Ni-base AM combustor alloy under *in-phase* and *out-of-phase* TMF loading with respect to maximum temperature and specimen orientation relative to the building direction. However, they did not report on the influence on lifetime. In order to apply AM materials for critical hot-going components, deeper insights into their TMF behaviour are necessary. In this study, we investigate the TMF deformation, damage and lifetime behaviour of 316L stainless steel manufactured by laser powder bed fusion. TMF tests under *in-phase* and *out-of-phase* conditions on specimens with loading axis parallel and transverse to the building direction were conducted, respectively. The results are discussed based on the microstructural and damage evolution. The goal is to reveal the mechanisms governing the relationship between specimen orientation, phase angle and resulting lifetime. The insights may allow for an AM building strategy, which provides an optimized microstructure for specific TMF loading conditions in service.

2. Material and methods

2.1. Specimen manufacturing

In this study, austenitic stainless steel 316L manufactured by laser powder bed fusion (L-PBF 316L) was fatigued in a variable temperature field. In conventionally manufactured form, 316L steel is commonly used in energy conversion industry for manufacturing of critical hot-going components such as the pipelines, impellers or heat exchangers due to its good corrosion resistance and high temperature strength. The material was supplied in the form of bars which were manufactured using an SLM Solutions SLM 280 HL machine with a single 400 W laser. The powder particles were spherical with diameters in the range of 10–45 μm. A common bidirectional scanning strategy with a 67° interlayer rotation was adopted. The layer thickness was 30 μm. Solid round specimens with a gauge length of 15 mm and a gauge length diameter of 5 mm were machined out of the bars and their surfaces ground to Ra = 0.4 μm. The surface quality of the raw specimens has thus no influence on the test results. This study considers the AM microstructure, not the surface. Two types of specimens were prepared, considering the inclination of the loading axis (LA) to the building

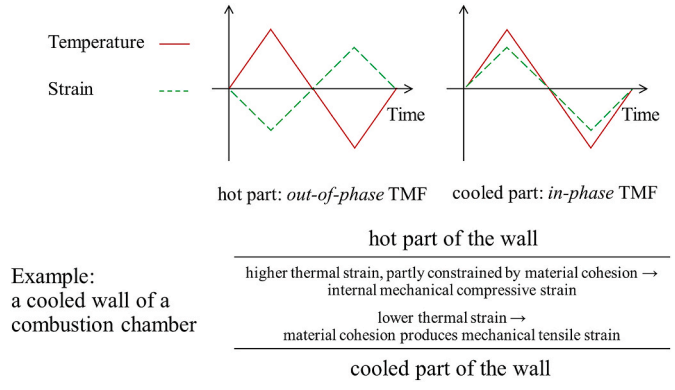

Fig. 1. Schematic illustration on the origin of TMF loading in hot-going components.

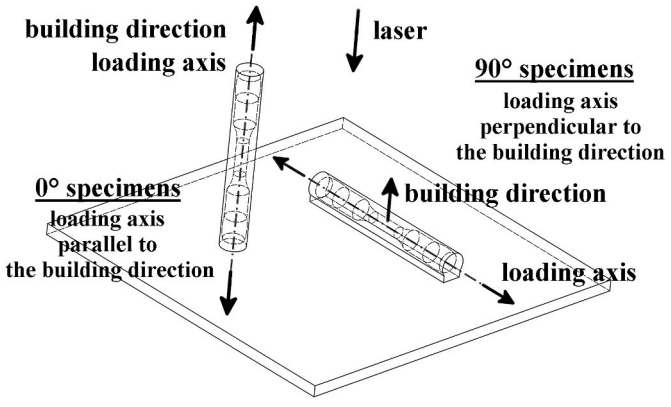

Fig. 2. Schematic showing the two adopted specimen orientations – 0° and 90°, relating the specimen loading axis to the building direction.

direction (BD) – 0° and 90°, as illustrated in Fig. 2. The chemical composition of the supplied alloy listed in Table 1 was measured using a glow discharge optical emission spectrometer GD-Profiler 2 by Horiba. Stress-relieving annealing was performed for 2 h at 600 °C prior to TMF testing.

2.2. Thermomechanical fatigue testing

Prior to the testing, Young's moduli of the individual specimens were evaluated at room temperature from the unloading curve of a 2.5 kN load, which produced a stress of about 130 MPa in the material, hence safely in the elastic region. The final values were evaluated as an average of 3 consecutive measurements. The TMF tests were performed under total mechanical strain control on a computer-controlled servoelectric Zwick testing machine in laboratory air. Total strain was measured using a high temperature extensometer, which was applied using alumina rods. The specimens were heated by an induction system using a copper coil. Cooling was realized by thermal conduction into the water-cooled grips. The cyclic straining was uniaxial and fully reversed ($R = -1$) with a triangular cycle shape. Simultaneously to the strain cycling, the temperature was cycled between 550 and 750 °C with a temperature rate of 6.7 °C/s, giving a cycle time of 60 s. The test temperature range was chosen to meet demanding conditions for potential applications in energy conversion. Investigated phase angles between mechanical and thermal cycling were 0° (*in-phase* loading) and 180° (*out-of-phase* loading), see Fig. 1. The TMF lifetime (cycles to failure) N_f was determined using a 10% drop of the stabilized maximum stress as failure criterion. The applied total mechanical strain amplitudes ranged from $\varepsilon_a^{mech} = 0.2–0.6\%$, resulting in lifetimes between about 50 and 4000 cycles, respectively.

2.3. Microstructural characterization

After the tests, the specimens were cut transversally and longitudinally to investigate the microstructure and TMF damage evolution. The cuts were mechanically polished and etched with Beraha colour etchant and documented using an optical microscope Olympus GX51. For a detailed analysis, the specimens were observed using scanning electron microscope (SEM) LYRA 3 XMU FEG/SEMxFIB equipped with an energy-dispersive spectrometer (EDS) Oxford Instruments X-MAX 80 and electron backscatter diffraction (EBSD) detector Symmetry by Oxford Instruments. EBSD (controlled using AZtec system) was utilized for texture analysis, phase analysis, grain boundary analysis and selection of suitable grains for cell size analysis. Cell size analysis was performed on <100> grains (10° deviation was accepted) using linear intercept method on SEM images covering the area of 2000x2000 μm^2. Thin foils were prepared and analysed using transmission electron microscopy (TEM) in systems JEOL JEM-2100F equipped with an EDS detector Oxford Instruments X-MAX 80 and Thermo Scientific Talos F200i with built-in EDS detector. Both TEM systems enabled observations in scanning mode (STEM).

3. Results

3.1. Initial state

The density of the specimens was established using the Archimedes method. Considering a reference value of 7.98 g/cm^3, the relative density was 99.34 ± 0.08% and 99.28 ± 0.06% for the 0° and the 90° specimen orientation, respectively. The measurement of machined specimens was complicated by trapped air bubbles in the centre bore due to machining, slightly lowering the measured values. Neither a metallographic inspection nor additional computed tomography analyses revealed any lack-of-fusion defects; inherent porosity was found to be spherical.

Optical microscopy micrographs shown in Fig. 3a and b revealed the microstructure (highlighted by Beraha etchant) of both 0° and 90° specimens in the initial state. The melt pool pattern corresponding to the L-PBF procedure is well visible for both specimen orientations. Fig. 3a shows elongated features corresponding to the laser movement during the manufacturing. These features should not be mistaken for grains, which are elongated in the building direction as apparent from a detail in Fig. 3b. The shades of blue correspond to the individual melt pools. TEM micrographs shown in Fig. 3c and d reveal the unique feature of L-PBF 316L microstructure, namely the submicron honeycomb-like dislocation cell structure elongated along a <100> direction. The microstructure was thus hierarchical in nature comprising grains, separated by high-angle grain boundaries (>10°; HAGB), subgrains separated by low-angle grain boundaries (2–10°; LAGB) and solidification/dislocation cells with a misorientation typically smaller than 1° (see Ref. [23]). Phase content and microstructural texture were analysed in both transversal and longitudinal cuts by means of EBSD. The microstructure exhibits a <110> texture along the building direction (see Fig. 3e and f). More importantly, considering the loading direction, 0° specimens exhibited a strong <110> texture (as the loading axis is parallel to the building direction) with a maximum multiple of uniform density of 5.86.90° specimen orientation exhibited a moderate <100> texture with a maximum multiple of uniform density of 2.82 along the loading axis. The microstructure was almost solely austenitic with nano-sized ferritic crystallites occasionally (up to 0.5%) present at the grain boundaries. Room temperature Young's modulus was 215.2 ± 7.9 GPa and 207.3 ± 4.9 GPa for the 0° and the 90° specimen orientation, respectively.

3.2. Lifetime and cyclic response

Fig. 4a shows that the TMF lifetime behaviour varies under *in-phase* and *out-of-phase* loading with the specimen orientation. Considering the phase angle, *in-phase* TMF is more damaging and leads to shorter lifetimes. Considering the specimen orientation, the 90° specimen orientation is generally stronger, induces higher stresses and exhibits less plasticity as follows from Fig. 4b and c. For *in-phase* loading mode, 0° specimens exhibited significantly higher lifetimes. Although the resulting lifetimes for both specimen orientations were similar under *out-of-phase* loading mode, 90° specimens performed markedly better than the 0° specimens, when considering the much higher resulting stress amplitudes for 90° specimens.

Fig. 4d shows a comparison of cyclic hardening/softening curves at $\varepsilon_a^{mech} = 0.3\%$. Additionally, it shows a development of mean stresses during cycling, compressive for *in-phase* and tensile for *out-of-phase* loading modes, which is a typical feature of TMF tests [15,19,20]. This is caused by loading at different temperatures (see Fig. 1), resulting in a loading asymmetry since the material is softer at higher temperatures. Under *in-phase* TMF loading, the stress amplitude drops continuously until failure. Under *out-of-phase* TMF loading, the stress amplitude drops initially and saturates then until macroscopic crack initiation. Comparing the specimen orientations, the behaviour was similar, however 90° specimens exhibited a more stable response due to higher flow

Table 1
Chemical composition of L-PBF 316L in wt.% measured using glow discharge optical emission spectrometer.

Fe	Cr	Ni	Mo	Si	Mn	Co	Nb	Cu	P	S	N	C
Bal.	17.29	10.90	1.96	1.34	1.08	0.4	0.08	0.07	0.03	0.02	0.30	0.04

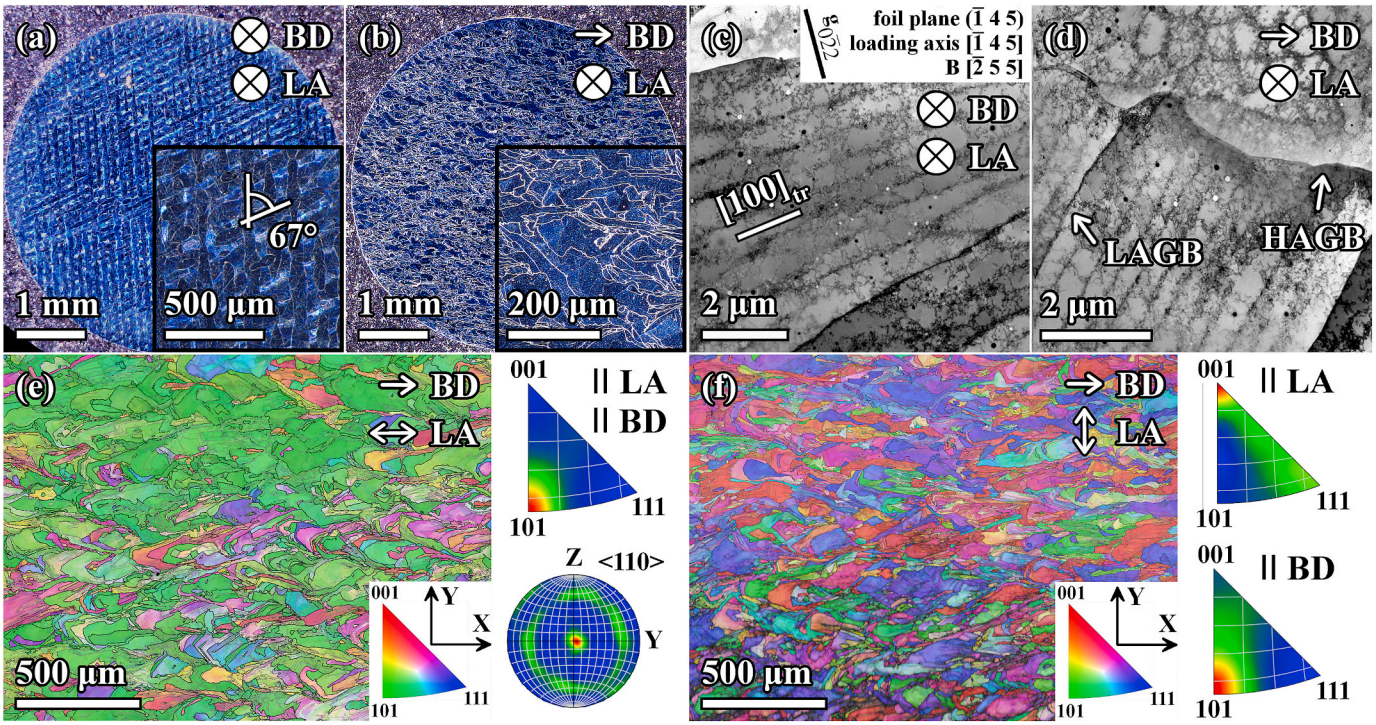

Fig. 3. Microstructural characteristics corresponding to the initial state of L-PBF 316L prior to the testing. (a–b) Optical microscopy micrographs of cross-sections etched with Beraha colour etchant, taken in polarized light contrast: (a) 0° specimen with a detail revealing the bidirectional scanning strategy with a 67° rotation between subsequent layers. (b) 90° specimen with a detail revealing grain elongation along the building direction (BD), different shades of blue correspond to melt pools. (c–d) STEM micrographs revealing cellular dislocation structure elongated along a <100> direction for (c) 0° specimen and (d) 90° specimen. (e–f) EBSD IPF maps complemented by pole and inverse pole figures, showing material texture along the loading axis (LA). (e) IPFX map; 0° specimen. (f) IPFY map; 90° specimen. (For interpretation of the references to colour in this figure legend, the reader is referred to the Web version of this article.)

stress and thus lower plasticity at a given strain amplitude (notice the narrower hysteresis loops corresponding to the 90° specimen orientation in Fig. 4c), manifested in a lower softening ratio as shown in Table 2. The softening ratios *SR* were calculated as follows:

$$SR = \frac{\sigma_{a,1} - \sigma_{a,50\%N_f}}{\sigma_{a,1}} \bullet 100\ [\%], \tag{1}$$

where $\sigma_{a,1}$ stands for stress amplitude in the first cycle and $\sigma_{a,50\%N_f}$ stands for stress amplitude at half-life. As follows from Table 2, softening ratios were found to be inversely proportional to the applied strain amplitude. At high strain amplitudes ($\varepsilon_a^{mech} \geq 0.5\%$) under *out-of-phase* TMF loading, the initial drop and saturation of the stress amplitude was followed by a continuous increase in stress amplitude until macroscopic crack initiation (i.e. cyclic hardening), manifested in negative values of softening ratios.

3.3. Damage observation and microstructure evolution

The character of damage was found to be independent on specimen orientation. Under *in-phase* TMF loading, the fracture surface was faceted (see Fig. 5a and in detail in Fig. 5b), indicating intergranular cracking. The facets were interconnected by short transgranular bridges as revealed by EBSD analysis in Fig. 5c and d. SEM analysis of longitudinal sections revealed an extensive intergranular crack network (see Fig. 5e). On one of the side crack branches, cavities were documented (Fig. 5g), and microcracks from coalesced cavities (Fig. 5h), which eventually connect to form the crack networks (Fig. 5e and f). Under *out-of-phase* TMF loading, the damage was mostly transgranular with striations on the fracture surface, indicating a microductile manner of the fracture, as shown in Fig. 6a and b. Crack initiation was abundant (see Fig. 6c) and the resulting cracks were relatively short. The specimen surface was oxidized as well as the crack surfaces (Fig. 6c). Also, internal damage was documented (Fig. 6d and e), indicating intergranular crack propagation in some areas.

The influence of the phase angle is reflected in the number of cycles to failure, or more precisely, the cumulative plastic strain ε_p^{cum}, and also in considerably different thermal exposure times during the tests. Qualitatively, the dislocation cell structure mostly remained stable throughout the high temperature *in-phase* TMF loading as shown from Fig. 7a. Table 3 shows only a minor increase in cell sizes after termination of the *in-phase* TMF tests. After *out-of-phase* TMF, the increase in cell size is more distinct for 0° specimens. The cellular structure witnessed a transformation from the initial honeycomb structure to less regular cellular shapes (see Fig. 8a and b). Favourably oriented grains witnessed heavy deformation resulting in more pronounced coarsening of the cellular structure as shown in Fig. 8a.

In addition to the changes in dislocation cell arrangement, some other features were observed, namely slip bands (Fig. 7c) running on {111} planes and deformation twins (Fig. 7d). Both features were observed rarely. In all the 18 observed TEM specimens, twins were found only in 2 grains and slip bands in 5 grains altogether.

Spherical Si/Mn oxide particles (confirmed by EDS analysis shown in Fig. 8d) up to 200 nm large showed a good stability and contributed to material strengthening via Orowan looping as shown in Fig. 7b. The distribution of the oxide particles was random. In addition to the oxide particles present already in the initial state of L-PBF 316L, TMF loading induced a time-dependent precipitation of elongated, usually sharp-edged particles. In relatively short-lived *in-phase* specimens, precipitation was observed exclusively at grain boundaries (HAGB) as shown in Fig. 7e. In relatively long-lived *out-of-phase* specimens, i.e. the specimens subjected to a longer thermal exposure, the precipitation occurred also at subgrain boundaries and cell walls (Fig. 8a, c) and oxide precursors (Fig. 8d). Some precipitates at grain boundaries coarsened up to 250 nm along the long edge, the majority fit within 50–100 nm.

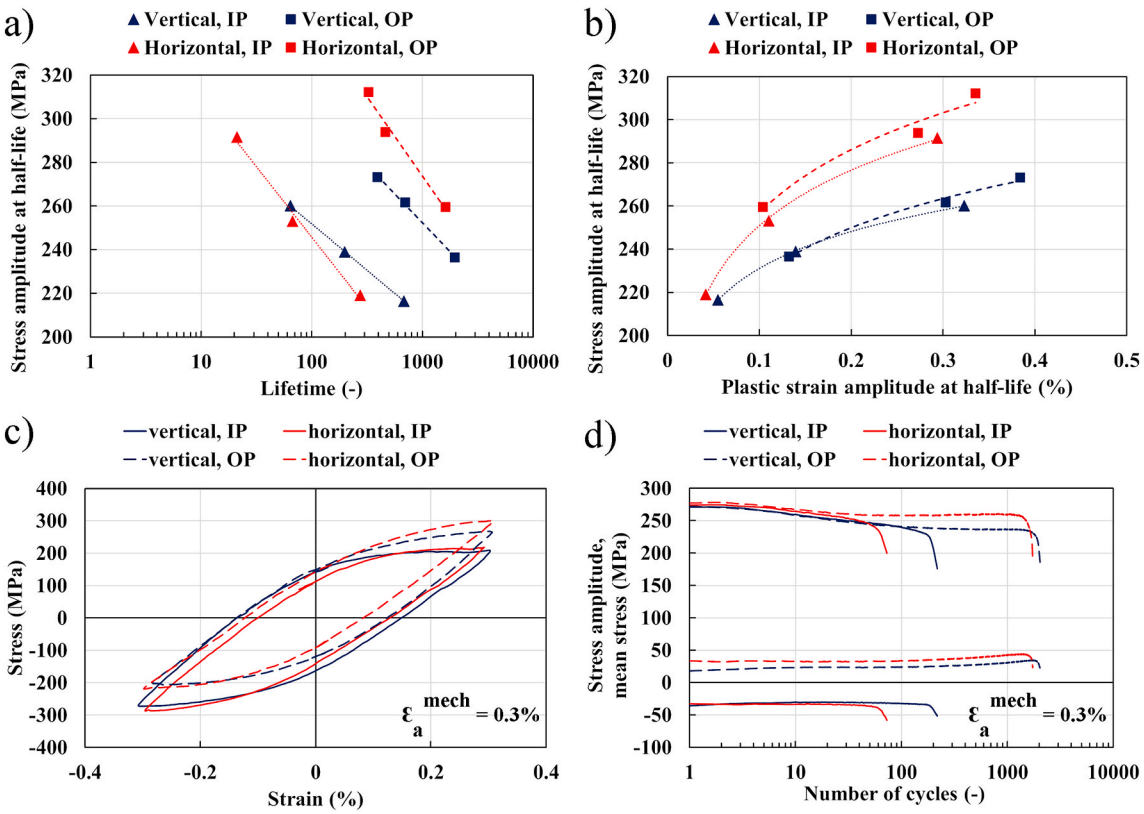

Fig. 4. Comparison of lifetime performance and cyclic stress-strain behaviour of L-PBF 316L of different specimen orientations subjected to *in-phase* (IP) and *out-of-phase* (OP) TMF loading. (a) Basquin-type lifetime representation showing the half-life stress amplitude vs. TMF lifetime. (b) Cyclic stress-strain curves showing the half-life stress amplitude vs. plastic strain amplitude. (c) Half-life hysteresis loops and (d) evolution of stress amplitudes and mean stresses during TMF cycling with total mechanical strain amplitude $\varepsilon_a^{mech} = 0.3\%$.

Table 2
Softening ratios evaluated for the conducted tests. Note that negative values correspond to the cyclic hardening occurring during TMF tests.

in-phase TMF			*out-of-phase* TMF		
ε_a^{mech}	*SR* (0° specimen)	*SR* (90° specimen)	ε_a^{mech}	*SR* (0° specimen)	*SR* (90° specimen)
0.20%	13.1%	8.1%	0.30%	13.0%	6.1%
0.30%	11.8%	7.8%	0.50%	8.8%	−2.2%
0.50%	6.2%	3.2%	0.60%	6.2%	−3.7%

Precipitates were often aligned in rows, following the cell walls in a <100> direction (Fig. 8c). EDS analysis shown in Figs. 7e and 8d revealed an enrichment in Mo and Si, in case of bigger particles also in Cr, and depletion of Fe and Ni.

4. Discussion

4.1. Deformation behaviour and microstructure

In comparison to conventional 316L [15,16], L-PBF 316L exhibits a more stable cyclic response during TMF. The reason is presumably the inherent cellular structure formed during the manufacturing [24], which, in principle, imposes thermomechanical loading on the component being built [25]. The general feature of both specimen orientations is the tendency to cyclic softening from the early stages of cycling which is typical for heavily-deformed stainless steels [26,27], and contrasts with pronounced initial cyclic hardening in solution annealed 316L steel [19]. Softening behaviour has been reported over various AM metals (see e.g. Refs. [28–30]), pointing out the initial high dislocation density as the precursor for the softening behaviour. At the given temperature range (above 550 °C), sessile dislocation movement is possible, enabling easier dislocation annihilation as well as rearrangement of the cellular structure. Although the cells appear to rearrange constantly during TMF loading (see Fig. 8a and b and the cell size change summarised in Table 3), the resulting dislocation structure does not change dramatically. The change in the cell size does not seem sufficient to have a significant influence on cyclic behaviour. Comparing our results with those of Li et al. [31], a decrease in dislocation density has clearly a stronger softening effect than the cell size change itself.

The specimen orientation affects the deformation behaviour on a quantitative basis, namely the level of cyclic stresses (Fig. 4b–d) and the evolution of softening ratios (Table 2), and also the cell size growth (Table 3). Our results document higher attained levels of cyclic stresses for the 90° specimen orientation, which is consistent with findings of Lindström et al. [22] on an AM Ni-based superalloy. The influence of specimen orientation can be reconciled with a study by Mineur et al. [32] on the effect of texture on cyclic stress-strain response of fatigued 316L steel produced conventionally. The authors showed that a <100> texture exhibit higher cyclic stresses than a <110> texture. This occurs due to the <100> direction favouring multiple slip while the <110> direction rather favours single slip [33]. It can thus be argued that a <100> texture, i.e., the 90° specimen orientation, exhibits a stronger hardening component competing with prevalent initial softening, which is altogether manifested in more stable cyclic response (compare the softening ratios in Table 2).

The evolution of stress amplitude, resulting in cyclic saturation or even hardening (manifested in negative values of softening ratio shown in Table 2) at the intermediate stage of life, indicates a gradual prevalence of a competing hardening mechanism. It is likely a result of several hardening effects. Firstly, there is an effect of multiple slip, which becomes stronger with increasing strain, resulting in more pronounced

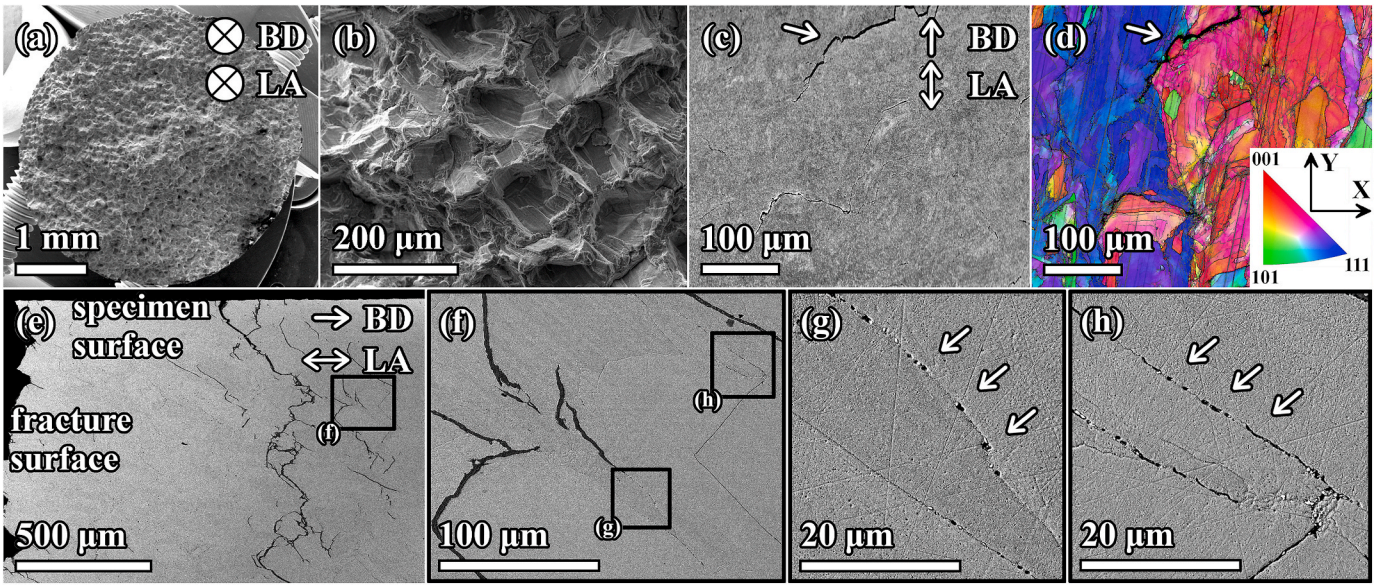

Fig. 5. SEM analyses of damage in L-PBF 316L due to *in-phase* TMF (0° specimen, $\varepsilon_a^{mech} = 0.3\%$, $N_f = 198$). (a–b) Fracture surface exhibiting numerous flat facets shown in detail in (b). (c–d) SEM micrograph and EBSD IPFX map of the identical area, showing mostly intergranular crack propagation with short transgranular bridges (see the crack pointed at by the arrow). (e–h) Creep damage mechanisms as documented on a longitudinal specimen section close to the fracture surface in detail: (e) overview with an extensive intergranular crack network, (f) detail of numerous, predominantly intergranular microcracks, (g) cavities at the grain boundaries, pointed out by arrows, and (h) coalescence of cavities into microcracks, pointed out by arrows.

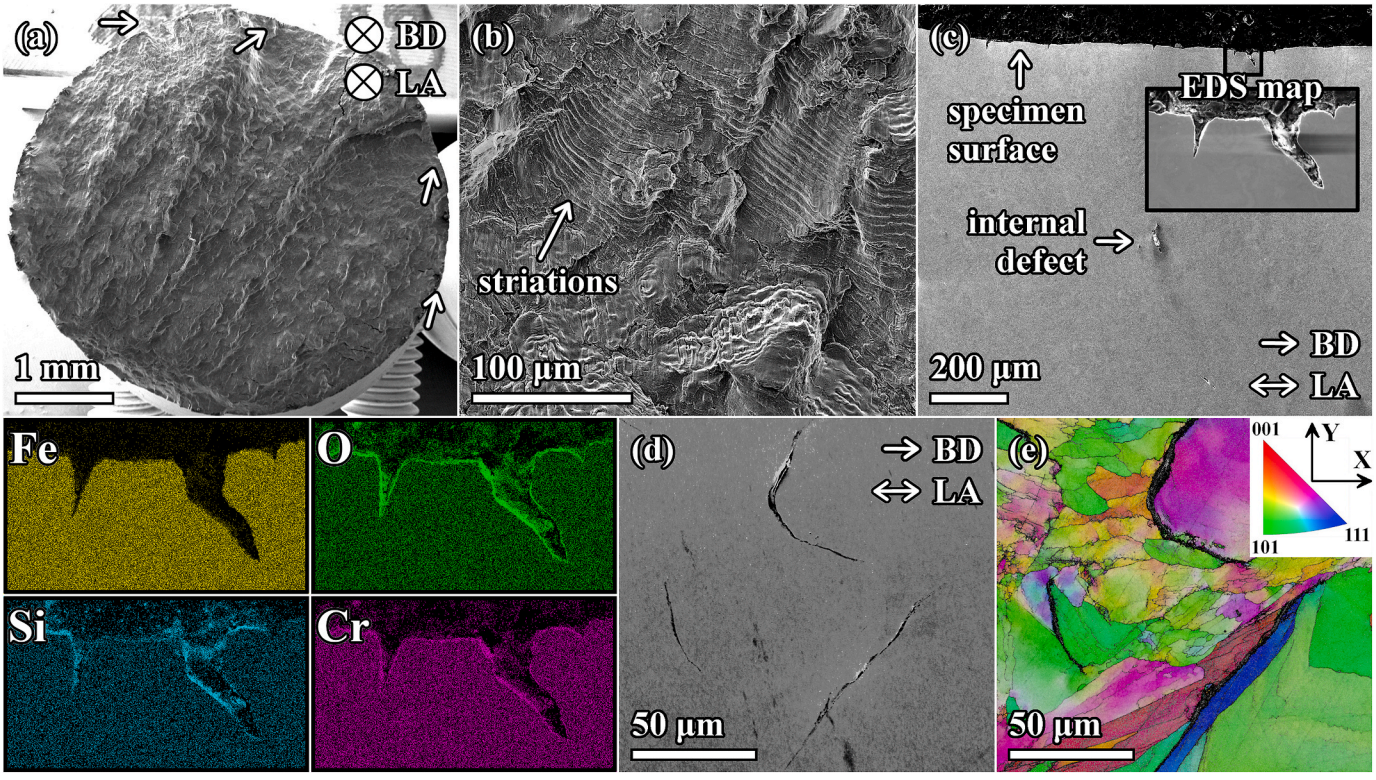

Fig. 6. SEM analyses of damage in L-PBF 316L due to *out-of-phase* TMF (0° specimen, $\varepsilon_a^{mech} = 0.3\%$, $N_f = 1952$). (a–b) Ductile fracture surface with multiple crack initiation sites and striations. (c) Multiple crack initiation sites at the specimen surface as documented on a longitudinal specimen section and EDS mapping of the selected area witnessing surface oxidation. (d–e) SEM micrograph and EBSD IPFX map of the identical area revealing intergranular cracking.

forest hardening. Another candidate is dynamic strain aging, which is known to decrease the softening ratio [27], in agreeement with our findings. Even though the stress response is smooth (see the hysteresis loops in Fig. 4c), the occurrence of dynamic strain aging is possible since planar slip was observed in the form of slip bands (see Fig. 7e–h).We assume the resulting effect is negligible due to scarcity of slip bands. Another contributing factor might be the frequent precipitation of Mo- and Si-enriched particles, acting as barriers to dislocation motion. The precipitates generally occur in the areas with high dislocation density; first at grain boundaries (high-angle grain boundaries), as can be seen on

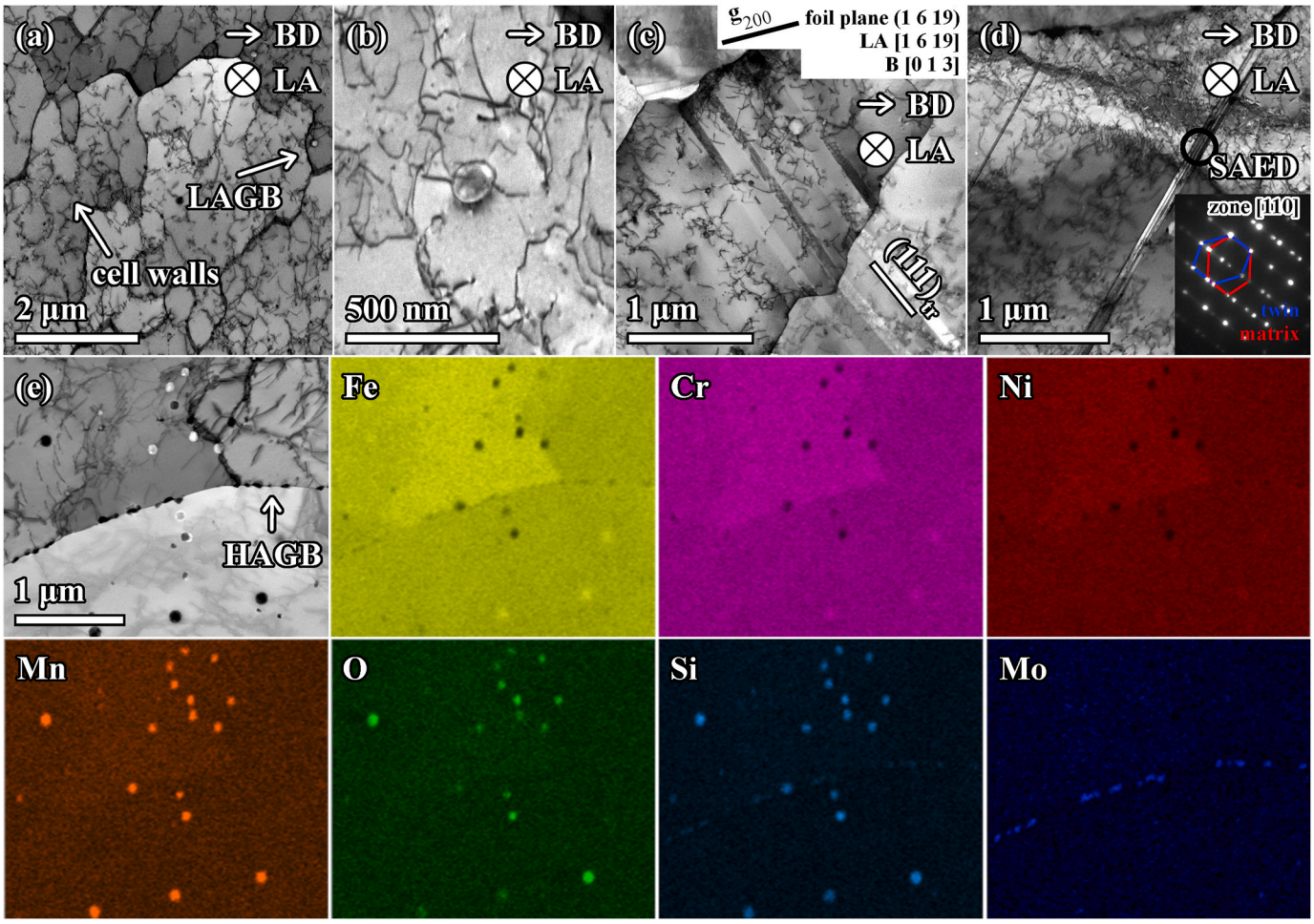

Fig. 7. TEM/STEM analyses of microstructural evolution in L-PBF 316L due to *in-phase* TMF (90° specimen, $\varepsilon_a^{mech} = 0.3\%$, $N_f = 67$). (a) The dislocation cell structure after cycling. Notice the fragmentation into subgrains separated by low-angle grain boundaries (LAGB). (b) Slip bands on {111} planes. (c) Orowan looping around an oxide particle. (d) Twinning documented by selected area diffraction (SAED) in [110] zone. (e) STEM + EDS analysis revealing Mn/Si oxides and Mo- and Si-enriched particles precipitated at grain boundaries (HAGB).

Table 3
A comparison of dislocation cell sizes in the initial state and post-mortem *in-phase* and *out-of-phase* TMF tests of L-PBF 316L, cycled with the identical total strain amplitude $\varepsilon_a^{mech} = 0.3\%$. The values were obtained using linear intercept method on SEM micrographs. Note that the comparison is rather illustrative as the microstructure is heavily directional.

	ε_p^{cum}	Cell size: 0° specimen (μm)	ε_p^{cum}	Cell size: 90° specimen (μm)
initial state		0.45 ± 0.09		0.50 ± 0.06
in-phase TMF	27.31%	0.46 ± 0.09	7.20%	0.50 ± 0.06
out-of-phase TMF	249.30%	0.53 ± 0.10	166.63%	0.51 ± 0.07

relatively short-lived *in-phase* specimens (see Fig. 7b). Later, they precipitate also intragranularly, at subgrain boundaries (low-angle grain boundaries), cell walls (Fig. 8a, d) and oxide precursors (Fig. 8d), as can be seen on *out-of-phase* specimens with relatively long fatigue lives. Due to grain and cell elongation, precipitates are often aligned in rows (Fig. 8c). Thermal stability tests on L-PBF 316L conducted by Yin et al. [34] indicate that the precipitates are $M_{23}C_6$-type carbides, complemented by σ-phase and/or Mo silicide. The assumption is partially supported by EDS analysis shown in Figs. 7e and 8d, revealing enrichment in Mo and Si, Cr too in case of bigger particles at grain boundaries, and depletion in Fe and Ni.

There are several other microstructural features occurring in the material as the result of the manufacturing process or the TMF testing. The random distribution of spherical Si/Mn oxides complement to material strength via the Orowan looping mechanism as shown in Fig. 7c. However, Wang et al. [1] found that the effect of oxide strengthening is negligibly small. Deformation twins were observed rarely (only in 2 grains altogether), hence cyclic hardening by twinning can be considered as negligible. Localisation into slip bands exhibited similar scarcity (5 grains in total) and it can thus be assumed that the corresponding softening effect is negligible too. The low occurrence of planar arrangements can be attributed to relatively high strains, in accordance with the study on the microstructural evolution during TMF of conventional 304L steel by Zauter et al. [35].

4.2. Damage and lifetime – influence of the phase angle

The observed behaviour of L-PBF 316L regarding the influence of the phase angle is in agreement with numerous previous studies on TMF behaviour of conventionally produced metals [13–20]. When the maximum temperature is sufficiently high to induce creep damage, *in-phase* TMF is generally more damaging than *out-of-phase* TMF because of creep-fatigue interactions under tensile load at the highest temperatures [15,16], which is also the case here. The resulting fracture surface after *in-phase* TMF loading was faceted (Fig. 5a and b), confirming intergranular crack propagation. This is in agreement with SEM

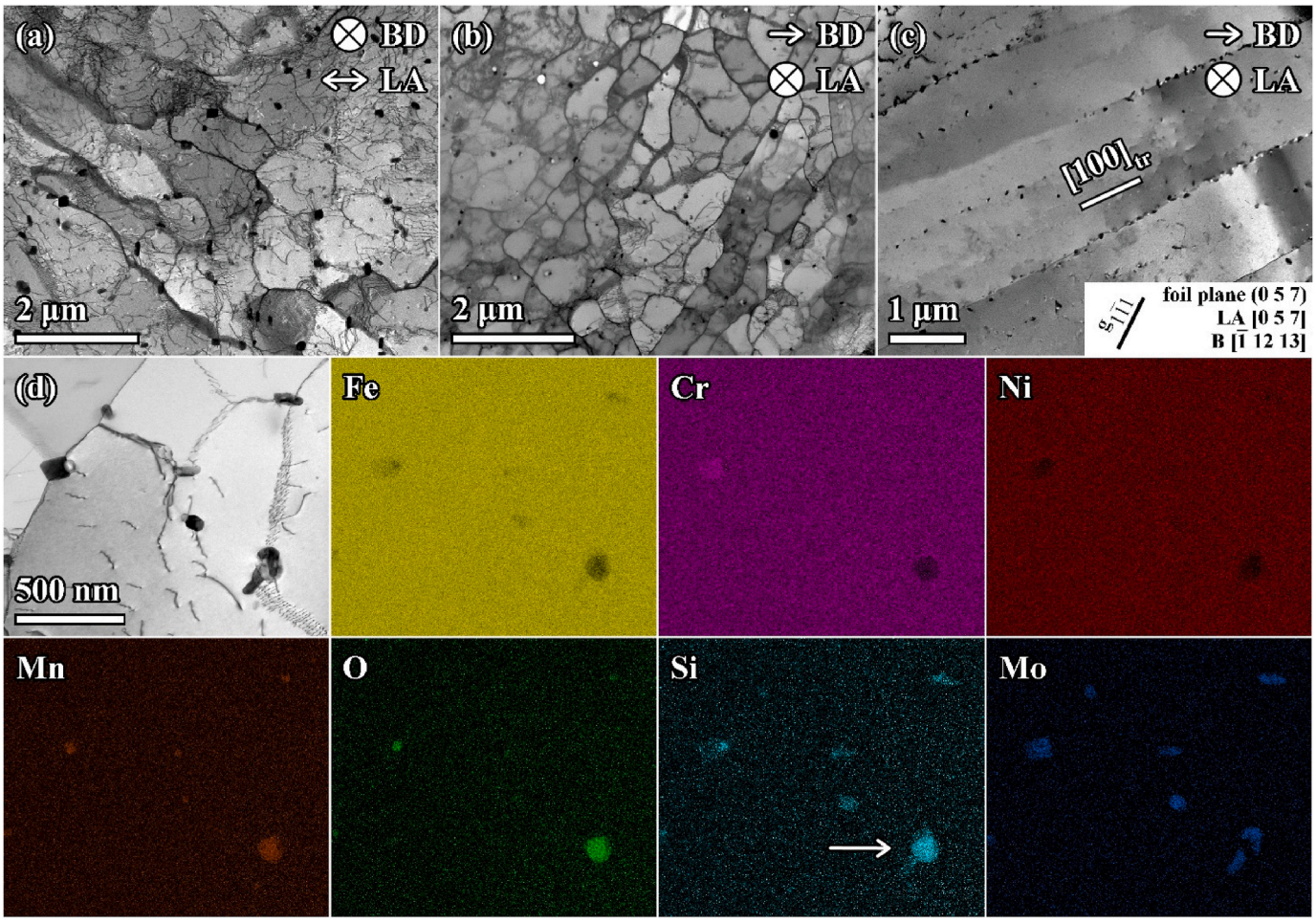

Fig. 8. STEM + EDS analyses of microstructural evolution in L-PBF 316L due to *out-of-phase* TMF (90° specimen, $\varepsilon_a^{mech} = 0.3\%$, $N_f = 1613$). (a) Heavily deformed microstructure with numerous sharp-edged, relatively coarse precipitates. (b) Well-defined dislocation cell structure comprising irregularly shaped cells which are non-uniform in size. (c) Row alignment of precipitates along subgrain boundaries and cell walls elongated along a <100> direction. (d) STEM + EDS analysis revealing Mn/Si oxides and Mo- and Si-enriched particles, the larger ones enriched also in Cr. The arrow points out the precipitation at an oxide precursor.

observations (Fig. 5e–h), showing creep damage by nucleation of cavities (Fig. 5g), which coalesced into microcracks (Fig. 5h), eventually forming extensive (Fig. 5e and f) internal crack networks. The intergranular cracking could be further accelerated by the precipitates at grain boundaries (see Fig. 7b) as suggested by Ávila Calderón et al. [36]. The evolution of internal crack networks gradually reduces the load-carrying cross-section, resulting in a gradual decrease of the stress amplitude as shown in Fig. 4d. Altogether, the lifetime of L-PBF 316L under *in-phase* TMF loading at the given temperature range is determined by an evolution of internal damage along grain boundaries, which outweighs possible life-prolonging effects of the compressive mean stress.

Under *out-of-phase* TMF, compressive creep inhibits the formation of cavities and even heals them out [37]. Internal damage may occur intergranularly (Fig. 6d and e) either due to grain boundary sliding [38] or due to tensile stresses at temperatures promoting creep damage. Because of its scarcity, internal damage had only a negligible impact on the material behaviour. The primary damaging mechanism was the stress-assisted surface oxide cracking, resulting in a large number of short cracks, which ran approximately perpendicular to the surface (see Fig. 6a, c). The reason for this are the relatively high tensile stresses at low temperatures, which easily crack the brittle oxide layer (Fig. 6d) formed at the surface. This is a typical *out-of-phase* TMF damage mechanism observed also in conventional alloys [14,18]. Hence, the lifetime of L-PBF 316L under *out-of-phase* TMF is determined by a growth of a principal crack growing transgranularly due to repeated cyclic plasticity [38]. It can be assumed that the tensile mean stress contributes to faster crack propagation and thus shorter lifetime.

4.3. Damage and lifetime – influence of the specimen orientation to the building direction

The lifetime curves shown in Fig. 4a demonstrate that either 0° or 90° specimen orientation can offer better performance regarding the TMF loading. Under *in-phase* TMF loading, higher lifetimes are achieved by the 0° specimen orientation, i.e., when the loading axis is parallel to the building direction. An extensive intergranular crack network forms, and the cracks are naturally most harmful when they are oriented perpendicular to the external tensile stress which acts as a crack opener. Due to the directionality of the microstructure, 90° specimen orientation exhibits relatively more grain boundaries perpendicular to the loading axis, resulting in relatively worse TMF properties under *in-phase* loading mode at the given temperature range.

In the absence of significant creep damage under *out-of-phase* TMF loading, the lifetime curves (Fig. 4a) show that the 90° specimen orientation performs markedly better than 0°, confirming the results of Afkhami et al. [8]. This can be explained again by the directionality of the microstructure; the two crucial factors are the material texture and the amount of grain boundaries in the direction of the load. It was shown by Mineur et al. [32] that <100> texture exhibits higher flow stress than

<110> texture in conventional 316L steel. Furthermore, the grain boundaries act as an impenetrable barrier to dislocation motion, resulting in dislocation pile-up formation at the boundaries. Hence more grain boundaries in the direction of the load corresponds to higher Hall-Petch strengthening for the 90° specimen orientation. The resulting higher flow stress explains the comparably lower plasticity of 90° specimens (see Fig. 4c) in strain cycling.

5. Conclusions

AM by laser powder bed fusion provides not only design freedom, crucial for manufacturing of complex-shaped components with internal features such as cooling pipes, but also, in the case of 316L austenitic stainless steel, a unique cellular microstructure. The most important findings regarding the TMF behaviour of L-PBF 316L steel are summarised as follows.

- The cellular dislocation arrangement shows good stability towards combined thermal loading up to 750 °C and severe plastic deformation with only minor cell coarsening. This is manifested in a more stable response to cyclic loading in comparison to the conventional 316L steel.
- Under *in-phase* TMF loading, the damage is mostly intergranular due to excessive creep damage while under *out-of-phase* TMF load, the damage is fatigue-dominated and thus mostly transgranular. The basic damage mechanisms as well as the lifetime behaviour of additively manufactured 316L steel correspond to those of conventionally manufactured material.
- Depending on the phase angle, either the 0° or the 90° specimen orientation, related to the inherently vertical building direction, offers better properties regarding the TMF loading. Under *in-phase* TMF load, 0° specimens perform better while under *out-of-phase* TMF load, 90° specimens perform better. Hence, with adapted design, AM offers the means to optimize the microstructure for the respective loading conditions in service. Since the key feature is the microstructural texture inherent due to the manufacturing process itself, we assume our findings may apply generally to L-PBF steels.

CRediT authorship contribution statement

T. Babinský: Conceptualization, Methodology, Investigation, Data curation, Writing – original draft, Writing – review & editing. **I. Šulák:** Investigation, Writing – review & editing. **I. Kuběna:** Investigation. **J. Man:** Writing – review & editing. **A. Weiser:** Resources. **E. Švábenská:** Investigation. **L. Englert:** Investigation. **S. Guth:** Conceptualization, Resources, Writing – review & editing, Supervision.

Declaration of competing interest

The authors declare that they have no known competing financial interests or personal relationships that could have appeared to influence the work reported in this paper.

Data availability

Data will be made available on request.

Acknowledgements

The authors would like to express gratitude to Siemens AG group T AMM COA-DE for providing the additively manufactured specimens and to Prof. Antonín Dlouhý for providing important insights. T. Babinský would like to thank the Ministry of Education, Youth and Sports of the Czech Republic for supporting a 3-month-long research stay at the Karlsruhe Institute of Technology through the Project No. CZ.02.2.69/0.0/0.0/18_053/0016933. The research was financially supported by H2020-WIDESPREAD-2018-03 under the grant agreement No. 857124, the Twinning project on the Structural Integrity and Reliability of Advanced Materials obtained through additive Manufacturing (SIRAMM).

References

[1] Y.M. Wang, T. Voisin, J.T. McKeown, J. Ye, N.P. Calta, Z. Li, Z. Zeng, Y. Zhang, W. Chen, T.T. Roehling, R.T. Ott, M.K. Santala, P.J. Depond, M.J. Matthews, A. V. Hamza, T. Zhu, Additively manufactured hierarchical stainless steels with high strength and ductility, Nat. Mater. 17 (2018) 63–71, https://doi.org/10.1038/nmat5021.

[2] E. Liverani, S. Toschi, L. Ceschini, A. Fortunato, Effect of selective laser melting (SLM) process parameters on microstructure and mechanical properties of 316L austenitic stainless steel, J. Mater. Process. Technol. 249 (2017) 255–263, https://doi.org/10.1016/j.jmatprotec.2017.05.042.

[3] L. Liu, Q. Ding, Y. Zhong, J. Zou, J. Wu, Y.-L. Chiu, J. Li, Z. Zhang, Q. Yu, Z. Shen, Dislocation network in additive manufactured steel breaks strength–ductility trade-off, Mater. Today 21 (2018) 354–361, https://doi.org/10.1016/j.mattod.2017.11.004.

[4] P. Kumar, R. Jayaraj, J. Suryawanshi, U.R. Satwik, J. McKinnell, U. Ramamurty, Fatigue strength of additively manufactured 316L austenitic stainless steel, Acta Mater. 199 (2020) 225–239, https://doi.org/10.1016/j.actamat.2020.08.033.

[5] L. Cui, S. Jiang, J. Xu, R.L. Peng, R.T. Mousavian, J. Moverare, Revealing relationships between microstructure and hardening nature of additively manufactured 316L stainless steel, Mater. Des. 198 (2021), https://doi.org/10.1016/j.matdes.2020.109385.

[6] L. Cui, D. Deng, F. Jiang, R.L. Peng, T. Xin, R.T. Mousavian, Z. Yang, J. Moverare, Superior low cycle fatigue property from cell structures in additively manufactured 316L stainless steel, J. Mater. Sci. Technol. 111 (2022) 268–278, https://doi.org/10.1016/j.jmst.2021.10.006.

[7] Y. Chen, X. Wang, J. Shen, Y. Peng, Y. Jiang, X. Yang, S.B. Leen, J. Gong, Deformation mechanisms of selective laser melted 316L austenitic stainless steel in high temperature low cycle fatigue, Mater. Sci. Eng. 843 (2022), https://doi.org/10.1016/j.msea.2022.143123.

[8] S. Afkhami, M. Dabiri, S.H. Alavi, T. Björk, A. Salminen, Fatigue characteristics of steels manufactured by selective laser melting, Int. J. Fatig. 122 (2019) 72–83, https://doi.org/10.1016/j.ijfatigue.2018.12.029.

[9] H. Gong, K. Rafi, H. Gu, G.D. Janaki Ram, T. Starr, B. Stucker, Influence of defects on mechanical properties of Ti–6Al–4V components produced by selective laser melting and electron beam melting, Mater. Des. 86 (2015) 545–554, https://doi.org/10.1016/j.matdes.2015.07.147.

[10] J. Polák, J. Man, Mechanisms of extrusion and intrusion formation in fatigued crystalline materials, Mater. Sci. Eng. 596 (2014) 15–24, https://doi.org/10.1016/j.msea.2013.12.005.

[11] H. Mughrabi, Microstructural mechanisms of cyclic deformation, fatigue crack initiation and early crack growth, Philos. Trans. R. Soc. A. Math. Phys. Eng. Sci. 373 (2015), https://doi.org/10.1098/rsta.2014.0132.

[12] K. Saeidi, X. Gao, F. Lofaj, L. Kvetková, Z.J. Shen, Transformation of austenite to duplex austenite-ferrite assembly in annealed stainless steel 316L consolidated by laser melting, J. Alloys Compd. 633 (2015) 463–469, https://doi.org/10.1016/j.jallcom.2015.01.249.

[13] S. Guth, K.-H. Lang, Influence of dwell times on microstructure, deformation and damage behavior of NiCr22Co12Mo9 under thermomechanical fatigue, Mater. Sci. Eng. 794 (2020), https://doi.org/10.1016/j.msea.2020.139970.

[14] R. Petráš, I. Šulák, J. Polák, The effect of dwell on thermomechanical fatigue in superaustenitic steel Sanicro 25, Fatig. Fract. Eng. Mater. Struct. 44 (2021) 673–688, https://doi.org/10.1111/ffe.13385.

[15] R. Zauter, H.J. Christ, H. Mughrabi, Some aspects of thermomechanical fatigue of AISI 304L stainless steel: Part I. Creep-fatigue damage, Metall. Mater. Trans. 25 (1994) 401–406, https://doi.org/10.1007/BF02647985.

[16] A. Nagesha, R. Kannan, P. Parameswaran, R. Sandhya, K.B.S. Rao, V. Singh, A comparative study of isothermal and thermomechanical fatigue on type 316L(N) austenitic stainless steel, Mater. Sci. Eng. 527 (2010) 5969–5975, https://doi.org/10.1016/j.msea.2010.05.082.

[17] D.A. Boismier, H. Sehitoglu, Thermo-mechanical fatigue of mar-m247: Part 1—experiments, J. Eng. Mater. Technol. 112 (1990) 68–79, https://doi.org/10.1115/1.2903189.

[18] S. Guth, S. Doll, K.-H. Lang, Influence of phase angle on lifetime, cyclic deformation and damage behavior of Mar-M247 LC under thermo-mechanical fatigue, Mater. Sci. Eng. 642 (2015) 42–48, https://doi.org/10.1016/j.msea.2015.06.055.

[19] H.-J. Shi, Z.-G. Wang, H.-H. Su, Thermomechanical fatigue of a 316L austenitic steel at two different temperature intervals, Scripta Mater. 35 (1996) 1107–1113, https://doi.org/10.1016/1359-6462(96)00254-0.

[20] A. Nagesha, M. Valsan, R. Kannan, K. Bhanusankararao, V. Bauer, H. Christ, V. Singh, Thermomechanical fatigue evaluation and life prediction of 316L(N) stainless steel, Int. J. Fatig. 31 (2009) 636–643, https://doi.org/10.1016/j.ijfatigue.2008.03.019.

[21] V.A. Popovich, E.V. Borisov, V. Heurtebise, T. Riemslag, A.A. Popovich, V. S. Sufiiarov, Creep and thermomechanical fatigue of functionally graded inconel 718 produced by additive manufacturing, in: TMS 2018 147Th Annual Meeting & Exhibition Supplemental Proceedings, Springer International Publishing, Cham, 2018, pp. 85–97, https://doi.org/10.1007/978-3-319-72526-0_9.

[22] T. Lindström, D. Nilsson, K. Simonsson, R. Eriksson, J.-E. Lundgren, D. Leidermark, Constitutive model for thermomechanical fatigue conditions of an additively manufactured combustor alloy, Mech. Mater. 168 (2022), https://doi.org/10.1016/j.mechmat.2022.104273.
[23] S. Chen, G. Ma, G. Wu, A. Godfrey, T. Huang, X. Huang, Strengthening mechanisms in selective laser melted 316L stainless steel, Mater. Sci. Eng. 832 (2022), https://doi.org/10.1016/j.msea.2021.142434.
[24] Z. Li, Y. Cui, W. Yan, D. Zhang, Y. Fang, Y. Chen, Q. Yu, G. Wang, H. Ouyang, C. Fan, Q. Guo, D.-B. Xiong, S. Jin, G. Sha, N. Ghoniem, Z. Zhang, Y.M. Wang, Enhanced strengthening and hardening via self-stabilized dislocation network in additively manufactured metals, Mater. Today 50 (2021) 79–88, https://doi.org/10.1016/j.mattod.2021.06.002.
[25] G. Wang, H. Ouyang, C. Fan, Q. Guo, Z. Li, W. Yan, Z. Li, The origin of high-density dislocations in additively manufactured metals, Mater. Res. Lett. 8 (2020) 283–290, https://doi.org/10.1080/21663831.2020.1751739.
[26] S. Ganesh Sundara Raman, K.A. Padmanabhan, Effect of prior cold work on the room-temperature low-cycle fatigue behaviour of AISI 304LN stainless steel, Int. J. Fatig. 18 (1996) 71–79, https://doi.org/10.1016/0142-1123(95)00078-X.
[27] S.-G. Hong, S.-B. Lee, Dynamic strain aging under tensile and LCF loading conditions, and their comparison in cold worked 316L stainless steel, J. Nucl. Mater. 328 (2004) 232–242, https://doi.org/10.1016/j.jnucmat.2004.04.331.
[28] S. Gribbin, J. Bicknell, L. Jorgensen, I. Tsukrov, M. Knezevic, Low cycle fatigue behavior of direct metal laser sintered Inconel alloy 718, Int. J. Fatig. 93 (2016) 156–167, https://doi.org/10.1016/j.ijfatigue.2016.08.019.
[29] J.S. Jesus, L.P. Borrego, J.A.M. Ferreira, J.D. Costa, C. Capela, Fatigue behavior of Ti6Al4V alloy components manufactured by selective laser melting subjected to hot isostatic pressing and residual stress relief, Fatig. Fract. Eng. Mater. Struct. 44 (2021) 1916–1930, https://doi.org/10.1111/ffe.13450.
[30] C.-H. Yu, A. Leicht, R.L. Peng, J. Moverare, Low cycle fatigue of additively manufactured thin-walled stainless steel 316L, Mater. Sci. Eng. 821 (2021), https://doi.org/10.1016/j.msea.2021.141598.
[31] Z. Li, B. He, Q. Guo, Strengthening and hardening mechanisms of additively manufactured stainless steels: the role of cell sizes, Scripta Mater. 177 (2020) 17–21, https://doi.org/10.1016/j.scriptamat.2019.10.005.
[32] M. Mineur, P. Villechaise, J. Mendez, Influence of the crystalline texture on the fatigue behavior of a 316L austenitic stainless steel, Mater. Sci. Eng. 286 (2000) 257–268, https://doi.org/10.1016/S0921-5093(00)00804-2.
[33] T.K. Lepistö, V.-T. Kuokkala, P.O. Kettunen, Dislocation arrangements in cyclically deformed copper single crystals, Mater. Sci. Eng. 81 (1986) 457–463, https://doi.org/10.1016/0025-5416(86)90283-1.
[34] H. Yin, M. Song, P. Deng, L. Li, B.C. Prorok, X. Lou, Thermal stability and microstructural evolution of additively manufactured 316L stainless steel by laser powder bed fusion at 500–800 °C, Addit. Manuf. 41 (2021), https://doi.org/10.1016/j.addma.2021.101981.
[35] R. Zauter, H.-J. Christ, H. Mughrabi, Some aspects of thermomechanical fatigue of AISI 304L Stainless Steel: Part II. dislocation arrangements, Metall. Mater. Trans. 25 (1994) 408–413, https://doi.org/10.1007/BF02647986.
[36] L.A. Ávila Calderón, B. Rehmer, S. Schriever, A. Ulbricht, L. Agudo Jácome, K. Sommer, G. Mohr, B. Skrotzki, A. Evans, Creep and creep damage behavior of stainless steel 316L manufactured by laser powder bed fusion, Mater. Sci. Eng. 830 (2022), https://doi.org/10.1016/j.msea.2021.142223.
[37] J.D. Whittenberger, M.V. Nathal, D.J. Gaydosh, Compressive and tensile creep in Fe-40Al-0.1Zr-0.4B at 1100 K, Intermetallics 2 (1994) 193–200, https://doi.org/10.1016/0966-9795(94)90058-2.
[38] S. Guth, K.-H. Lang, An approach to lifetime prediction for a wrought Ni-base alloy under thermo-mechanical fatigue with various phase angles between temperature and mechanical strain, Int. J. Fatig. 99 (2017) 286–294, https://doi.org/10.1016/j.ijfatigue.2016.10.015.